RSC Advances

PAPER

View Article Online
View Journal | View Issue

Cite this: *RSC Adv.*, 2018, **8**, 23599

Fabrication of nitrogen-doped ZnO nanorod arrays by hydrothermal synthesis and ambient annealing†

Ryosuke Kobayashi, [a] Tetsuo Kishi, [a] Yuta Katayanagi, [b] Tetsuji Yano[a] and Nobuhiro Matsushita *[a]

Received 16th May 2018
Accepted 18th June 2018

DOI: 10.1039/c8ra04168g

rsc.li/rsc-advances

Nitrogen-doped ZnO nanorod arrays (N:ZnO NRAs) were fabricated by hydrothermal synthesis using a zinc–ammine complex solution, followed by annealing at elevated temperatures under ambient conditions. After annealing at 400 °C for 1 h, Raman spectra indicated that nitrogen was incorporated in the ZnO crystal structure. NH_3-ligands in the zinc–ammine complex precursor were incorporated in ZnO crystals during hydrothermal crystal growth and were then ruptured during annealing. Photoluminescence spectra indicated that during post-annealing, the nitrogen was incorporated into the oxygen site, which created accompanying defects such as oxygen vacancies and/or interstitial oxygen. The absorption edge in diffuse-reflectance UV-visible spectra revealed visible absorption after post-annealing. In addition, the N:ZnO NRAs generated strong visible-light-induced photocurrents. Nitrogen doping caused a decline in carrier density, as confirmed by an electrochemical Mott–Schottky plot. These results suggest that this cost-effective fabrication has many potential applications such as solar-induced water splitting.

Introduction

Zinc oxide (ZnO) has many superior properties such as a wide, direct band gap, a large exciton binding energy, and high carrier mobility. Consequently, it has many applications.[1–3] Moreover, one-dimensional ZnO nanostructures have high charge-carrier diffusion lengths, low grain boundaries, and a high surface-to-volume ratio, which are essential features for many optoelectronic applications.[4–10] Photoelectrochemical water splitting under solar light has been explored extensively because of environmental issues.[11,12]

In general, undoped ZnO is only active under ultraviolet light. To make it reactive to visible light, doping is a commonly used to modify its optoelectronic properties. In particular, nitrogen doping reduces the absorption energy and enables ZnO to absorb visible light.[13] Hence, it is expected that nitrogen-doped ZnO nanorod arrays (N:ZnO NRAs) will be used for visible-light-reactive photoelectrodes.[14]

Typical N:ZnO NRAs fabrication involves dry processes, such as chemical vapor deposition[15] and pulsed laser deposition,[16] which require high-vacuum and high-temperature systems. Wet processes are much easier for fabricating undoped ZnO NRAs,[17,18] and offer cost-efficiency and the potential for large-scale production. Generally, wet fabrication of N:ZnO NRAs requires two steps: a solution process, followed by post-doping *via* annealing in an ammonia gas atmosphere.[14] Alternatively, ion implantation[19] is used to incorporate nitrogen without changing the nanostructure. However, the dopant distribution within the crystal cannot be effectively controlled with annealing in ammonia gas,[20,21] and complex, expensive systems are required for ion implantation.[19] It is thus desirable to establish an easy, cost-effective method to fabricate uniformly nitrogen-doped N:ZnO NRAs.

Here, N:ZnO NRAs were fabricated by combining hydrothermal synthesis using a zinc–ammine complex solution, and post-annealing in an ambient atmosphere. The zinc–ammine complex solution was chosen as a precursor for the hydrothermal synthesis because it provided nitrogen sources *via* the NH_3 ligands. The process was simple, and did not require specialized equipment or conditions. N:ZnO NRAs were obtained by annealing as-grown samples above 400 °C; visible light photocurrents were maximized when the sample was annealed at 500 °C. The nitrogen doping mechanism was as follows: (1) NH_3 ligands in the zinc–ammine complex were incorporated in ZnO crystals during the hydrothermal crystal growth; (2) the ligands dissociated during annealing; and (3) nitrogen doping occurred within the ZnO crystals. Defect formation mechanisms followed by annealing were also investigated.

[a]*Department of Materials Science and Engineering, School of Materials and Chemical Technology, Tokyo Institute of Technology, 2-12-1 Ookayama, Meguro-ku, Tokyo 152-8550, Japan. E-mail: matsushita.n.ab@m.titech.ac.jp; Fax: +81-3-5734-3353; Tel: +81-3-5734-2875*

[b]*Department of Technology Education, Faculty of Education, Gunma University, 4-2 Aramaki-machi, Maebashi, Gunma 371-8510, Japan*

† Electronic supplementary information (ESI) available. See DOI: 10.1039/c8ra04168g

Experimental

Preparation of zinc–ammine complex solution

$Zn(NO_3)_2 \cdot 6H_2O$ (>99%), NaOH (>97%), and NH_3 aqueous solution (28%), all from Wako Pure Chemical Industries, Ltd., Japan, were used without further purification. A zinc–ammine complex precursor solution was prepared according to Meyers *et al.*[22] Specifically, 10 ml of aqueous 2.5 M NaOH was added dropwise to 15 ml of aqueous 0.5 M $Zn(NO_3)_2 \cdot 6H_2O$ under vigorous stirring. The resulting slurry was centrifuged and the supernatant was removed. Rinsing and centrifugation was performed four times to remove Na^+ and NO_3^-. The precipitate was then dissolved in 50 ml of aqueous 6.6 M NH_3 to yield the zinc–ammine complex solution.

Preparation of ZnO seed layer

ZnO seed layers were deposited on a 20 mm × 30 mm FTO glass substrate (Sigma Aldrich, ~7 Ω sq^{-1}) by spin-coating the zinc–ammine complex solution. The substrate was first ultrasonically cleaned in acetone, then ethanol, and finally in distilled water for 10 min each. Then, the substrate was exposed to UV–ozone (ProCleaner™ Plus, Bioforce Nanosciences) for 10 min to produce a hydrophilic surface. The spin-coating was performed at 3000 rpm for 30 s. The substrate was then heated on a hot plate at 150 °C for 5 min. The spin-coating and heating steps were repeated ten times to get the desired ZnO thickness.

Fabrication of N-doped ZnO nanorod arrays

The zinc–ammine complex solution was diluted by a factor of three with distilled water to form a growth solution. The substrate was placed in a Teflon vessel and 30 ml of the growth solution was added. The vessel was covered, tightly enclosed in a stainless autoclave, and placed in an oven. The hydrothermal reaction was performed at 100 °C for 24 h. The substrates were then removed and immediately rinsed with distilled water. Then the samples were dried in an oven at 100 °C for 10 min, and annealed at 300–700 °C with a programming rate of 10 °C min^{-1}.

Characterization

Crystal phases were determined by X-ray diffraction (XRD), (Bruker D8, Bruker), using Cu Kα radiation. Sample morphologies were imaged with field-emission scanning electron microscopy (FE-SEM) (S-4500, Hitachi). Diffuse reflectance spectra were recorded with a UV-vis spectrophotometer (V-670, JASCO), using $BaSO_4$ as a reference material. Raman spectra were recorded with a Nanofinder30 spectrometer, using 532 nm excitation from a Nd:YAG laser. Photoluminescence (PL) spectra were recorded at room temperature with 325 nm excitation from a He-Cd laser. X-ray photoelectron spectroscopy (XPS) spectra were recorded on a Perkin-Elmer model 5500 MT XPS system, using monochromatic Al Kα radiation. Binding energies were calibrated with respect to the C 1s core level at 284.8 eV.

Photoelectrochemical experiments

Photoelectrochemical characteristics were measured with a potentiostat (HZ-7000, Hokuto Denko), using a standard three-electrode cell under visible light irradiation from a 100 W xenon lamp equipped with a <422 nm cutoff filter (Asahi Spectra). N:ZnO NRAs on FTO substrates were used as working electrodes with an effective area of 4 cm^2. A Pt plate and an Ag/AgCl electrode were used as counter and reference electrodes, respectively. A 0.1 M Na_2SO_4 aqueous solution was used as the electrolyte and was purged with Ar bubbling for 30 min before the experiments. Electrochemical impedance spectroscopy (EIS) was performed in a 0.5 M Na_2SO_4 electrolyte solution with a 5 mV amplitude, a 20 kHz to 1 Hz frequency range, and a potential range of −0.6 to 1.0 V *vs.* Ag/AgCl. Experimental setups are shown in Fig. S1.†

Results and discussion

Fig. 1 shows the XRD patterns of as-grown N:ZnO NRAs and those annealed at 500 °C for 1 h. The peaks were identified as würtzite-type ZnO (JCPDS 36-1451), with no observed impurity phases. In particular, the (002) peak was the strongest, indicating preferential crystal orientation along the *c*-axis. This orientation has often been observed in solution-processed ZnO.[17,18] Cross-sectional and top-view SEM images of the as-grown and annealed N:ZnO NRAs are also shown in Fig. 1. Nearly vertically aligned N:ZnO NRAs were obtained on the FTO substrate; their morphologies were maintained during annealing at 500 °C. The average diameter and length of the rods were approximately 210 nm and 12 μm, respectively.

Fig. 2 shows Raman spectra of the N:ZnO NRAs for the as-grown sample and for those annealed at different temperatures. All the spectra were normalized with respect to the highest peak intensity at 437 cm^{-1}. This peak was observed for all samples, and was attributed to the characteristic vibration of the high-frequency E_2 mode for würtzite-phase ZnO.[23] Peaks at 330 cm^{-1} were from multiple phonon scattering E_2 (MP).[24]

Additional peaks at 275 cm^{-1}, 510 cm^{-1}, 582 cm^{-1}, 635 cm^{-1} emerged after annealing above 400 °C; they are usually attributed to N-related local vibrational modes in ZnO.[16,25–27] According to calculations by Friedrich *et al.*[24] the peak at 275 cm^{-1} may be assigned to a vibrational mode between zinc interstitials (Zn_i) and the nitrogen substitution of oxygen (N_O). It

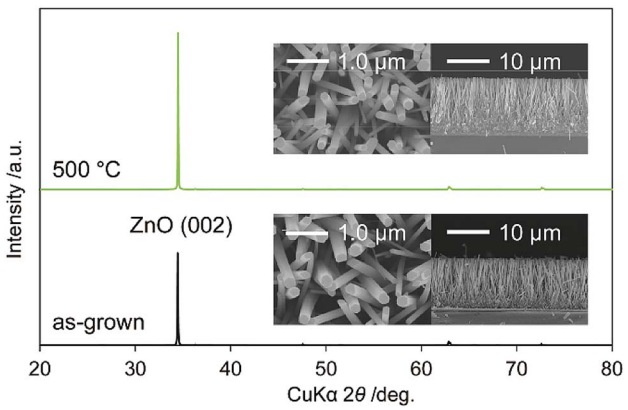

Fig. 1 XRD patterns of as-grown N:ZnO NRAs and those annealed at 500 °C for 1 h. Cross-sectional and top-view SEM images are shown in the insets.

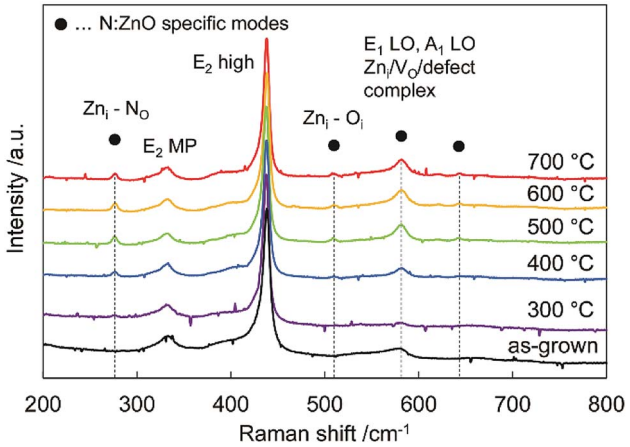

Fig. 2 Raman spectra of the as-grown N:ZnO NRA and those annealed at 300–700 °C for 1 h. All the spectra were normalized with respect to the peak intensity at 437 cm^{-1}.

emerged after annealing above 400 °C, and thus indicated that nitrogen was incorporated into the oxygen site. The peak at 581 cm^{-1} was assigned to an A1 longitudinal optical peak derived from defects such as an oxygen vacancy (Vo), Zn_i, and defect complexes in ZnO.[28,29] It disappeared after annealing at 300 °C, and appeared again after annealing above 400 °C. This result indicates that crystallinity was improved by annealing at 300 °C; whereas, new defects were created by nitrogen doping at annealing temperatures > 400 °C.

Fig. 3(a) shows the 275 cm^{-1} peaks in the Raman spectra fitted by Gaussian functions (dotted lines). Fig. 3(b) plots the calculated areas of the 275 cm^{-1} peaks *vs.* annealing temperature. The peak area increased with temperature, reached a maximum at around 500 °C, and then decreased above 600 °C. The peak intensity was a function of nitrogen dopant concentration.[30,31] When annealing temperature < 400 °C, N–H bonds were not sufficiently broken; thus, N-related peaks were not observed. Temperatures above 400 °C were sufficient to rupture N–H bonding. The nitrogen remained in the crystal, while the hydrogen eventually diffused out.[32]

To investigate sample defects, room-temperature PL spectroscopy was performed (Fig. 4). A strong near-band-edge luminescence at 380 nm is usually observed in ZnO,[33] but was suppressed and very weak in all the samples. This suggested that the samples had many defects, decreasing band-to-band transitions, and increasing band-to-defect level transitions or defect level-to-band transitions. The origin of the broad visible luminescence has been controversial because of its complexity. Generally, the violet emission originates from Zn_i-to-valence band transitions,[34] the yellow emission originates from OH groups made in the solution process,[35] the orange emission originates from conduction band or Zn_i-to-oxygen interstitials (O_i),[36] and the red emission originates from the conduction band-to-V_O or V_O-to-valence band transitions.[37,38] Tarun *et al.* reported that the red emission originated from a nitrogen dopant state.[39]

In the as-grown sample, there were many OH group/V_O defects remaining in the crystal, thus there was yellow/red

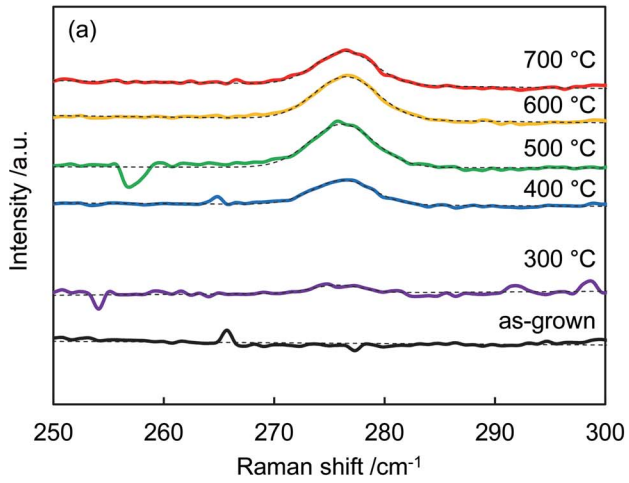

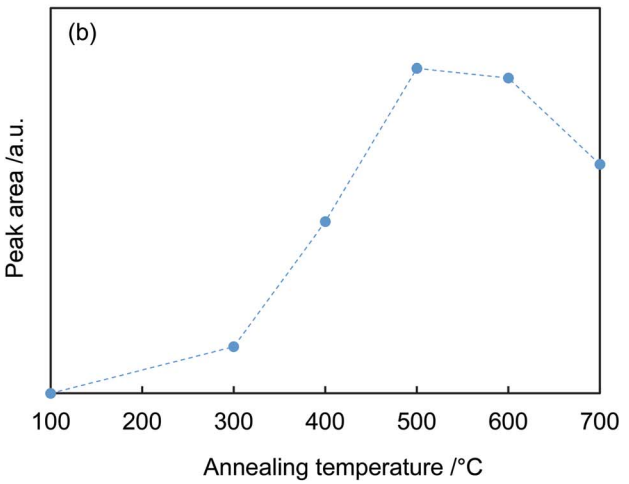

Fig. 3 (a) Raman spectra from Fig. 2 centered around 275 cm^{-1} and Gaussian fits. (b) Peak areas around 275 cm^{-1} *vs.* annealing temperature.

emission in the spectra. Annealing at 300 °C reduced the number of OH groups/V_O defects, decreasing the intensity of yellow/red luminescence. After 500 °C annealing, the O_i/V_O defects increased because of N doping at oxygen sites,

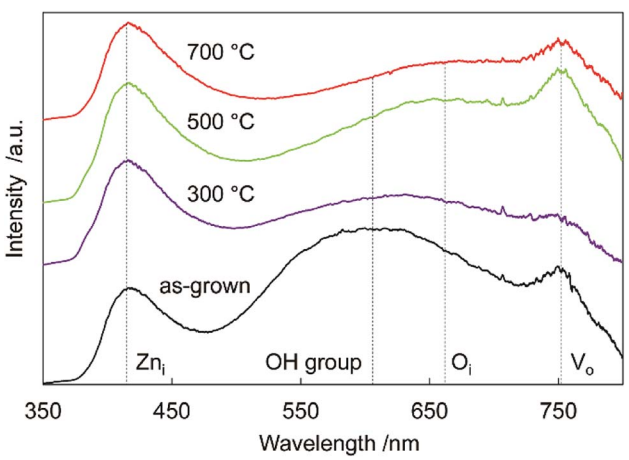

Fig. 4 Photoluminescence spectra of N:ZnO NRAs after various annealing temperatures.

increasing the orange/red luminescence. Annealing at 700 °C reduced all the defects in the crystal, and the total luminescence decreased. These results were supported by the Raman spectra (Fig. 2), which revealed the existence of Zn_i, O_i, and V_O defects. Differential scanning calorimetry (DSC) measurement of the sample also suggested the reduction of oxygen vacancies and the decomposition of the incorporated ammonia. More detailed thermal analysis is under investigation.

Diffuse reflectance absorption spectra of the N:ZnO NRAs are shown in Fig. 5. Before annealing, the absorption edge shifted to longer wavelengths relative to that reported for ZnO (~380 nm). This red shift was due to V_O defect levels created by NH_3 ligand incorporation, consistent with Raman and photoluminescence spectra (Fig. 2 and 4). Similar absorption shifts induced by oxygen vacancies have been previously reported and applied in visible-light-reactive photocatalysts.[40–42] After annealing at 300 °C, the absorption edge shifted to shorter wavelengths, similar to that previously reported for ZnO. Ambient annealing improved crystallinity and decreased the number of V_O defects. Therefore, the absorption edge shift that had been caused by V_O defects shifted back to the normal value for ZnO. After annealing at >400 °C, a broad shoulder absorption appeared around 500 nm that was attributed to the impurity levels formed by N doping.[42] These changes in visible light absorption were consistent with color changes of the samples from pale-yellow (as-grown) to white (annealed at 300 °C) and to pale orange (annealed >500 °C), as shown in Fig. S2.†

XPS spectra of the N 1s core levels for the samples are shown in Fig. 6. All the N 1s spectra exhibited single broad peaks, and they were deconvoluted into two peaks centered at 398.9 and 399.8 eV. The peaks around 398.9 eV were from nitrogen atoms in NH_3,[42,43] and the peaks around 399.8 eV were resulted from the formation of O–Zn–N bonds in the crystal.[19,21,44] The intensity of O–Zn–N related peak increased after annealing at 500 °C. This result suggested that N was doped at the O sites in ZnO after 500 °C annealing, which strongly supports our discussion on nitrogen doping mechanism. Peak around 404 eV was not observed in the spectra. This peak has been assigned to $(N_2)_O$,[45,46] thus the absence of the peak suggested the incorporated nitrogen was not from N_2 molecule in the atmosphere, but from NH_3 in the growth solution. The surface atomic ratio of N to Zn in the sample increased from 2.1% to 3.1% to 3.2% and to 4.7% in the as-grown sample and that annealed at 300 °C, 500 °C and 700 °C. This result suggests that nitrogen was incorporated inside the crystal during the crystal growth, and it thermally diffused from inside to the surface during the annealing.

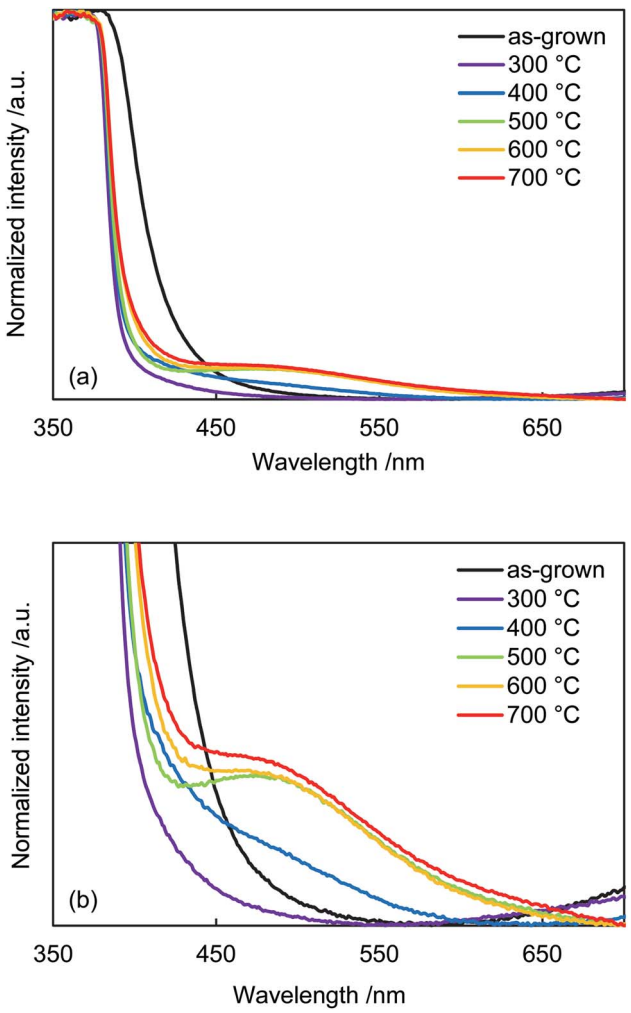

Fig. 5 (a) Diffuse-reflectance UV-vis spectra of as-grown N:ZnO NRAs and those annealed at 300–700 °C for 1 h. (b) Enlarged spectra from (a).

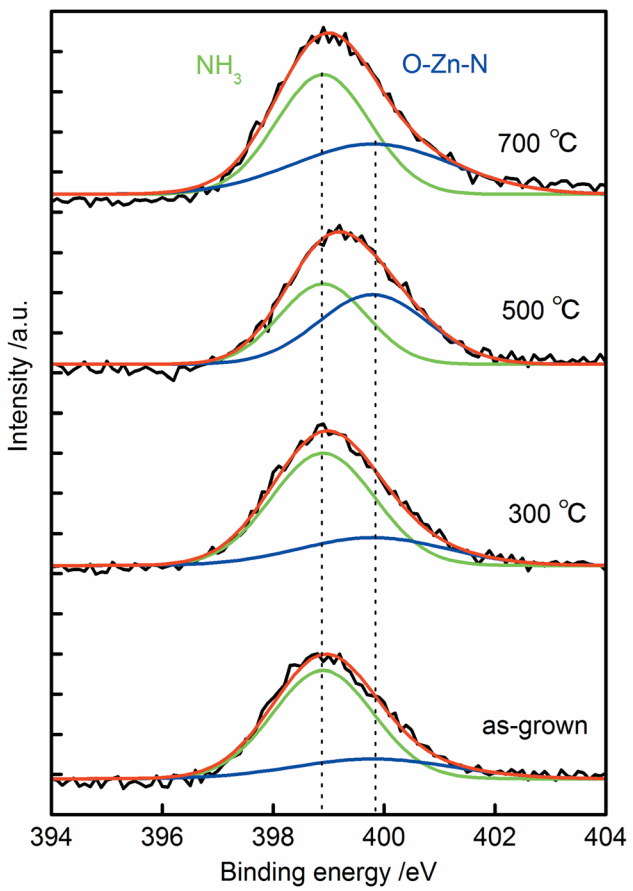

Fig. 6 XPS spectrum of the N 1s region of as-grown N:ZnO NRAs and those annealed at 300–700 °C for 1 h.

Fig. 7 shows photocurrent *vs.* time (*I*–*t*) measurements at 0.8 V recorded on N:ZnO NRAs with light on/off cycles using 422 nm illumination. The data show a very low dark current of $<10^{-7}$ A cm^{-2}. Upon illumination, an initial spike was observed in the photocurrent because of a power transient; the photocurrent then quickly relaxed to a steady-state value. The spikes were caused by photoexcited holes at electrode/electrolyte interfaces or at the interfaces within electrodes, which verified the existence of surface trap states in the sample.[19] The maximum photocurrent occurred in the sample annealed at 500 °C. This was over 18 times that for the as-grown sample, which exhibited very low photocurrent. The relationship between photocurrent density and annealing temperature correlated with the 275 cm^{-1} Raman peak intensities.

To determine the carrier density and the flat-band potential of the N:ZnO NRAs, Mott–Schottky analysis was performed using EIS. For flat electrodes, the Mott–Schottky equation is expressed by:

$$\frac{1}{C^2} = \frac{2}{qN_D\varepsilon_{ZnO}\varepsilon_0 A^2}(V - V_{fb}) \quad (1)$$

where C is the capacitance, q is the electron charge (1.6×10^{-19} coulomb), N_D is the apparent donor density, ε_{ZnO} is the dielectric constant of ZnO (10),[47] ε_o is the permittivity of free space (8.85×10^{-14} farad-cm^{-1}), A is the active electrode surface area, V is the applied voltage, and V_{fb} is the flat-band potential. The capacitance C was calculated by fitting the spectra with the equivalent circuit of the photoanode, which was $L_s + R_s+(R_H//\mathrm{CPE_H})+(R_{sc}//\mathrm{CPE_{sc}})$. Here, L_s/R_s was the inductance/resistance in the electrolyte or electrical contact. The parallel circuit of resistance R_H and the constant phase element $\mathrm{CPE_H}$ represented the Helmholtz layer at the ZnO/electrolyte interface, and the parallel circuit of R_{sc} and $\mathrm{CPE_{sc}}$ represented the space-charge layer at the ZnO/electrolyte interface. Usually, the capacitance in a space-charge layer is much smaller than that in a Helmholtz layer, therefore that in the Helmholtz layer can be neglected in a Mott–Schottky plot.

The impedance of the constant-phase element Z_{CPE} was:

$$Z_{CPE} = \frac{1}{(j\omega)^p T} \quad (2)$$

where T was the CPE prefactor, ω was the angular frequency ($2\pi f$), p was $0 \le p \le 1$, and j was an imaginary number. The value of C could be determined directly from T when $p = 1$. Here, p was almost constant over the entire voltage range in the space-charge layer area, and average values for each sample were >0.9. Therefore, assuming that the electrode capacitance could be represented directly by T, the Mott–Schottky plot was constructed using T instead of C.

In Fig. 8 is plotted C^{-2} *vs.* V. The positive slopes suggested that all the N:ZnO NRAs were n-type semiconductors, despite the nitrogen doping. There were two main reasons for n-type N:ZnO in this experiment. First, there were a lot of compensating donor defects in the sample. According to the Raman and PL spectra (Fig. 2 and 4), the existence of Zn_i and V_O were suggested. These defects worked as electron donor and compensated the acceptor-nitrogen in the crystal. Second, the acceptor-nitrogen concentration was too low to turn n-type to p-type. The Raman peak intensities at 275 cm^{-1} (shown in Fig. 2) were weaker than those shown in the previous reports on p-type N:ZnO.[21,27] This peak is assigned to a vibrational mode between Zn_i and N_O, and thus it represents the amount of nitrogen in the crystal. The weak intensity of the peak insists low nitrogen concentration in the sample. To determine the apparent donor density N_D from the Mott–Schottky analysis, the active surface area was estimated. N:ZnO NRAs were deposited on a 4 cm^2 area, but the actual active surface area was much larger because of the side areas of the rod arrays. From the SEM image in Fig. 1, the actual surface area could be estimated from the rod lengths, diameters, and density. There were about 25×10^6 nanowires per cm^2, with an average radius $r = 210$ nm and an average length $h = 12$ μm. Assuming a cylindrical surface area ($A_{cylinder} = 2\pi r^2 + 2\pi rh$), a total active surface area of $A = 16.1$ cm^2 was determined.

The calculated donor densities and flat band potentials are listed in Table 1. A low carrier density was calculated for the as-

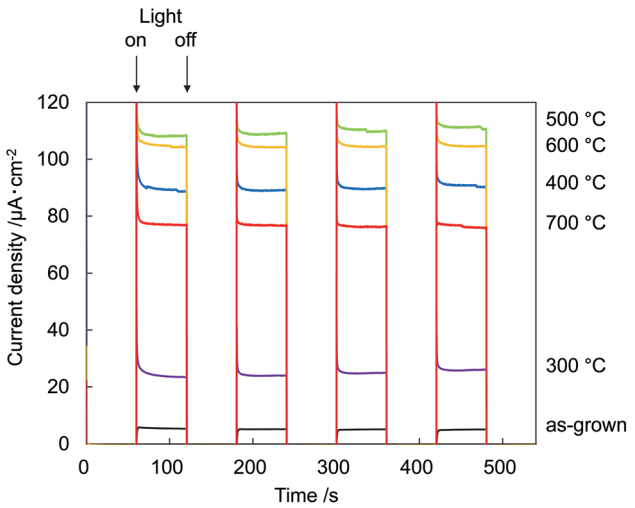

Fig. 7 Electrochemical *I*–*t* measurements recorded on N:ZnO NRAs with light on/off cycles at 0.8 V using >422 nm illumination.

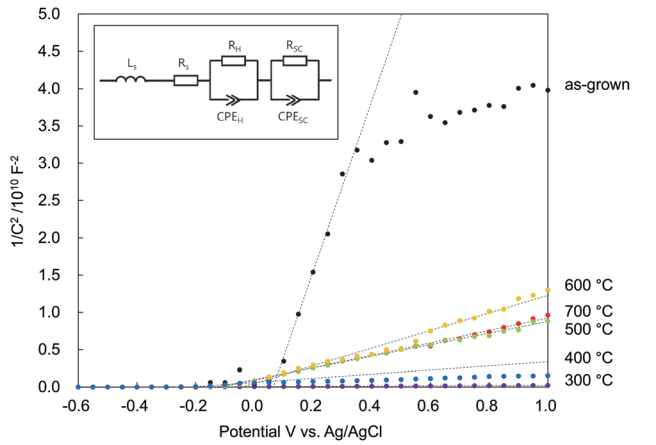

Fig. 8 Mott–Schottky plots of N:ZnO NRAs under dark conditions as a function of various annealing temperatures (inset: equivalent circuit of the photoanode used for the calculations).

Table 1 Calculated carrier densities and flat-band potentials from eqn (1) for N:ZnO NRAs after different annealing temperatures. A cylindrical approximation was used for estimating the surface area of N:ZnO NRAs

Sample	Carrier density/cm^{-3}	Flat band potential/ V *vs.* Ag/AgCl
As-grown	4.76×10^{17}	0.065
300 °C	3.16×10^{20}	−0.293
400 °C	1.96×10^{19}	−0.218
500 °C	7.00×10^{18}	−0.128
600 °C	4.61×10^{18}	−0.041
700 °C	6.55×10^{18}	−0.110

grown sample because there were many defects revealed in the PL spectra. After annealing at 300 °C, the defect density was reduced and trapped electrons were released; thus, the donor density increased sharply. However, the donor density decreased after annealing above 500 °C, indicating that doped nitrogen acted as an accepter in the ZnO. The donor density continuously decreased up to 600 °C and then increased again with annealing at 700 °C. This implied that the nitrogen accepter diminished at higher temperatures. The flat band potential was negatively shifted after annealing at 300 °C, and then positively shifted after annealing at 500 °C. These results indicated that electrons were released and that the Fermi level rose after 300 °C annealing, and then the doped nitrogen and the Fermi level fell again after >500 °C annealing.

Conclusion

N:ZnO NRAs were fabricated by hydrothermal synthesis using a zinc–ammine complex solution, followed by post-annealing at various temperatures under ambient conditions. Raman and photoluminescence spectra indicated that post-annealing dissociated the NH_3-ligands, allowing nitrogen to be incorporated at oxygen sites. When annealing occurred at a sufficiently high temperature, weak absorption appeared in the visible region (~500 nm). The N:ZnO NRAs generated strong visible-light-induced (>422 nm) photocurrents after post-annealing. This procedure requires neither expensive nor complex equipment, and thus should be applicable for large-scale fabrication of N:ZnO NRAs.

Conflicts of interest

There are no conflicts to declare.

Acknowledgements

This work was supported by MEXT Nanotechnology platform 12025014(F-17-IT-0017) for the micro structure images of samples. A part of this work was financially supported by Research Grant, The Murata Science Foundation. We thank Alan Burns, PhD, from the Edanz Group (https://www.edanzediting.com/ac) for editing a draft of this manuscript.

References

1 S. Liang, H. Sheng, Y. Liu, Z. Huo, Y. Lu and H. Shen, *J. Cryst. Growth*, 2001, **225**, 110–113.
2 J. Xu, Q. Pan and Z. Tian, *Sens. Actuators, B*, 2000, **66**, 277–279.
3 X. Jiang, F. Wong, M. Fung and S. Lee, *Appl. Phys. Lett.*, 2003, **83**, 1875–1877.
4 M. H. Huang, S. Mao, H. Feick, H. Yan, Y. Wu, H. Kind, E. Weber, R. Russo and P. Yang, *Science*, 2001, **292**, 1897–1899.
5 J. B. Baxter and E. S. Aydil, *Appl. Phys. Lett.*, 2005, **86**, 053114.
6 X. M. Zhang, M. Y. Lu, Y. Zhang, L. J. Chen and Z. L. Wang, *Adv. Mater.*, 2009, **21**, 2767–2770.
7 S.-J. Young, C.-C. Yang and L.-T. Lai, *J. Electrochem. Soc.*, 2017, **164**, B3013–B3028.
8 C.-L. Hsu, Y.-H. Lin, L.-K. Wang, T.-J. Hsueh, S.-P. Chang and S.-J. Chang, *ACS Appl. Mater. Interfaces*, 2017, **9**, 14935–14944.
9 T. Chen, S. Young, S. Chang, C. Hsiao and C. Huang, *J. Electrochem. Soc.*, 2012, **159**, J153–J157.
10 L.-W. Ji, C.-Z. Wu, C.-M. Lin, T.-H. Meen, K.-T. Lam, S.-M. Peng, S.-J. Young and C.-H. Liu, *Jpn. J. Appl. Phys.*, 2010, **49**, 052201.
11 A. Wolcott, W. A. Smith, T. R. Kuykendall, Y. Zhao and J. Z. Zhang, *Adv. Funct. Mater.*, 2009, **19**, 1849–1856.
12 H. M. Chen, C. K. Chen, Y. C. Chang, C. W. Tsai, R. S. Liu, S. F. Hu, W. S. Chang and K. H. Chen, *Angew. Chem.*, 2010, **122**, 6102–6105.
13 D. Li and H. Haneda, *J. Photochem. Photobiol., A*, 2003, **155**, 171–178.
14 X. Yang, A. Wolcott, G. Wang, A. Sobo, R. C. Fitzmorris, F. Qian, J. Z. Zhang and Y. Li, *Nano Lett.*, 2009, **9**, 2331–2336.
15 B. Xiang, P. Wang, X. Zhang, S. A. Dayeh, D. P. Aplin, C. Soci, D. Yu and D. Wang, *Nano Lett.*, 2007, **7**, 323–328.
16 B. Yang, P. Feng, A. Kumar, R. Katiyar and M. Achermann, *J. Phys. D: Appl. Phys.*, 2009, **42**, 195402.
17 M. Guo, P. Diao and S. Cai, *J. Solid State Chem.*, 2005, **178**, 1864–1873.
18 A. Sugunan, H. C. Warad, M. Boman and J. Dutta, *J. Sol-Gel Sci. Technol.*, 2006, **39**, 49–56.
19 M. Wang, F. Ren, J. Zhou, G. Cai, L. Cai, Y. Hu, D. Wang, Y. Liu, L. Guo and S. Shen, *Sci. Rep.*, 2015, **5**, 12925.
20 R. G. Palgrave, D. J. Payne and R. G. Egdell, *J. Mater. Chem.*, 2009, **19**, 8418–8425.
21 B. Chavillon, L. Cario, A. Renaud, F. Tessier, F. Cheviré, M. Boujtita, Y. Pellegrin, E. Blart, A. Smeigh and L. Hammarstrom, *J. Am. Chem. Soc.*, 2011, **134**, 464–470.
22 S. Meyers, J. Anderson, C. Hung, J. Thompson, J. Wager and D. Keszler, *J. Am. Chem. Soc.*, 2008, **130**, 17603–17609.
23 T. C. Damen, S. Porto and B. Tell, *Phys. Rev.*, 1966, **142**, 570.
24 F. Friedrich, M. Gluba and N. Nickel, *Appl. Phys. Lett.*, 2009, **95**, 141903.
25 A. Kaschner, U. Haboeck, M. Strassburg, M. Strassburg, G. Kaczmarczyk, A. Hoffmann, C. Thomsen, A. Zeuner,

H. Alves and D. Hofmann, *Appl. Phys. Lett.*, 2002, **80**, 1909–1911.
26 L. L. Kerr, X. Li, M. Canepa and A. J. Sommer, *Thin Solid Films*, 2007, **515**, 5282–5286.
27 N. P. Herring, L. S. Panchakarla and M. S. El-Shall, *Langmuir*, 2014, **30**, 2230–2240.
28 G. J. Exarhos and S. K. Sharma, *Thin Solid Films*, 1995, **270**, 27–32.
29 C. Youn, T. Jeong, M. Han and J. Kim, *J. Cryst. Growth*, 2004, **261**, 526–532.
30 J. Sann, J. Stehr, A. Hofstaetter, D. Hofmann, A. Neumann, M. Lerch, U. Haboeck, A. Hoffmann and C. Thomsen, *Phys. Rev. B: Condens. Matter Mater. Phys.*, 2007, **76**, 195203.
31 K. Jindal, M. Tomar, R. Katiyar and V. Gupta, *J. Appl. Phys.*, 2016, **120**, 135305.
32 J. Gao, X. Zhang, Y. Sun, Q. Zhao and D. Yu, *Nanotechnology*, 2010, **21**, 245703.
33 B. Meyer, H. Alves, D. Hofmann, W. Kriegseis, D. Forster, F. Bertram, J. Christen, A. Hoffmann, M. Straßburg and M. Dworzak, *Phys. Status Solidi B*, 2004, **241**, 231–260.
34 C. H. Ahn, Y. Y. Kim, D. C. Kim, S. K. Mohanta and H. K. Cho, *J. Appl. Phys.*, 2009, **105**, 013502.
35 A. Djurišić, Y. Leung, K. Tam, Y. Hsu, L. Ding, W. Ge, Y. Zhong, K. Wong, W. Chan and H. Tam, *Nanotechnology*, 2007, **18**, 095702.
36 X. Liu, X. Wu, H. Cao and R. Chang, *J. Appl. Phys.*, 2004, **95**, 3141–3147.
37 N. Alvi, K. Ul Hasan, O. Nur and M. Willander, *Nanoscale Res. Lett.*, 2011, **6**, 130.
38 F. Stavale, L. Pascua, N. Nilius and H.-J. Freund, *J. Phys. Chem. C*, 2014, **118**, 13693–13696.
39 M. Tarun, M. Z. Iqbal and M. McCluskey, *AIP Adv.*, 2011, **1**, 022105.
40 J. Wang, Z. Wang, B. Huang, Y. Ma, Y. Liu, X. Qin, X. Zhang and Y. Dai, *ACS Appl. Mater. Interfaces*, 2012, **4**, 4024–4030.
41 H.-L. Guo, Q. Zhu, X.-L. Wu, Y.-F. Jiang, X. Xie and A.-W. Xu, *Nanoscale*, 2015, **7**, 7216–7223.
42 X. Zong, C. Sun, H. Yu, Z. G. Chen, Z. Xing, D. Ye, G. Q. Lu, X. Li and L. Wang, *J. Phys. Chem. C*, 2013, **117**, 4937–4942.
43 X. Wang, J. C. Yu, Y. Chen, L. Wu and X. Fu, *Environ. Sci. Technol.*, 2006, **40**, 2369–2374.
44 L.-C. Chen, Y.-J. Tu, Y.-S. Wang, R.-S. Kan and C.-M. Huang, *J. Photochem. Photobiol., A*, 2008, **199**, 170–178.
45 K. Ahn, Y. Yan, S. Lee, T. Deutsch, J. Turner, C. Tracy, C. Perkins and M. Al-Jassim, *J. Electrochem. Soc.*, 2007, **154**, B956–B959.
46 C. Perkins, S. Lee, X. Li, S. Asher and T. Coutts, *J. Appl. Phys.*, 2005, **97**, 034907.
47 I. Mora-Seró, F. Fabregat-Santiago, B. Denier, J. Bisquert, R. Tena-Zaera, J. Elias and C. Lévy-Clément, *Appl. Phys. Lett.*, 2006, **89**, 203117.